

Tailoring the phase in nanoscale MoTe₂ grown by barrier-assisted chemical vapor deposition

*Christian Martella, Alessio Quadrelli, PinakaPani Tummala, Cristina Lenardi, Roberto Mantovan, Alessio Lamperti * and Alessandro Molle*

KEYWORDS molybdenum ditellurides, chemical vapor deposition, allotropic phase, MoTe₂.

ABSTRACT We employed chemical vapor deposition (CVD) from powder precursors aiming at large area growth of molybdenum ditellurides (MoTe₂) thin films, with controlled allotropic 2H and 1T' phases. This major outcome entails tuning the parametric conditions of the precursor fluxes during the deposition. Using a physical barrier, we induce a concentration gradient of the Te precursor thus enabling the control of the flux fluid-dynamics and the formation of a Te-rich or Te-poor environment. As a consequence, the allotropic phase repartition in the films turns out to be determined by the barrier-induced Te concentration, as clearly evidenced by statistical Raman scattering investigations. The effect of the physical barrier is also reflected in the shape of the crystallite population and in their log-normal areal distribution pointing out to a homogenous nucleation mode of the MoTe₂ crystals. Our approach shows the selective allotropic phase control in the barrier-assisted CVD deposition of MoTe₂ by adjusting the kinetics of the chemical reaction rather than with the use of growth surfactants.

Introduction

In the realm of two-dimensional (2D) transition metal dichalcogenides (TMDs), ditellurides, like MoTe_2 or WTe_2 , have recently gained an increasing interest for they host phase transitions through stable allotropic states with potential on nanoscience and nanotechnology.^{1,2} Transformation from the semiconducting 2H phase to the metallic 1T' one and vice versa is more readily facilitated in MoTe_2 , compared to other TMDs due to the relatively smaller energy barrier therein making it suitable as robust phase change building blocks in 2D non-volatile memory devices and memristors.^{3,4} Furthermore, the transformation from the semiconducting to the metallic phase, exploiting strategies like strain-engineering, envisages novel perspectives from nanoelectronics to the catalysis.⁵ The 1T' phase is also the precursor stage to access outstanding topological properties. In the latter respect, the 1T' phase in ditellurides, orthorhombic in structure, assumes a peculiar interest. At the single-layer stage, the 1T' phase hosts the quantum spin Hall effect, namely the hallmark of a 2D topological insulating state.^{6,7} At the multilayer level, the same phase is again the incubator of a 3D topological state, known as type-II Weyl semimetal, that takes place in the monoclinic T_d phase as a low-temperature distortion of the pristine 1T' phase.^{8,9}

Similar to other TMDs growth methods, chemical vapor deposition (CVD) is one of the best candidates aiming at a scalable production of ditellurides enabling the technological take-up of their peculiar physical and chemical properties. However, tailoring the growth process towards a full control of the phase variability gives a key-advantage with exploiting the full potential of ditellurides, but it is conditioned by the interplay of the thermodynamics and kinetics constraints in the CVD reaction. This fact is quite general for all TMDs, but the process parametric variability becomes particularly decisive in dictating the phase repartition in the ditellurides. This peculiarity is well-represented by case of the tellurization of a pre-deposited Mo, where one phase can be

controllably isolated from another essentially by means of time-dependent process parameters like the carrier gas flow.¹⁰ Such a phenomenology differentiates the details of tellurium reactivity at the Mo or MoO₃ base-plane from other chalcogen whose growth results in a polycrystalline layer with nanoscale grains^{11,12} and provides tips to reconsider the Te chemistry in other CVD processes. Usually, in sulphides and selenides the vapor phase reaction of the two components in the binary compound is the path to achieve nearly perfect 2H microscale crystals.^{13–15} Nevertheless, the vapor phase reaction from bare precursors (MoO₃ and Te) has so far received a relatively scarce consideration in the framework of the chemical vapor deposition of MoTe₂ owing to the difficulties in controlling Te chemistry in the process. Tellurium is less reactive than other chalcogens irrespectively of the reaction temperature, and the kinetic constraints during process makes phase tuning and, in particular, single phase isolation more elusive. To elucidate how phase transformations develop in this scenario, here we study a barrier-induced concentration gradient of the Te precursor. The target is to define the parametric conditions of the 1T'-MoTe₂ formation from a vapor phase reaction approach with no use of growth surfactants.¹⁶ We show that a mechanical barrier at the edge of the quartz boat accommodating the growth substrate is mandatory for the MoTe₂ growth to start up. In addition, we elucidate the details of the MoTe₂ nucleation in the aim to assess the stability of the 1T' phase against parametric variability of the process.

Materials and Methods

Materials growth

MoTe₂ crystals were grown on SiO₂ (50 nm)/Si substrate in a CVD apparatus (planarTECH LLC). A quartz tube was used as reaction chamber and two furnaces were used to set up upstream and downstream heating zones. In the upstream zone we loaded 100 mg of tellurium powder (99.998%,

Sigma-Aldrich), while ~24 cm away, in the downstream region, 1 mg of MoO₃ (99.98%, Sigma-Aldrich) was placed in a quartz boat. The substrate was placed directly on top of the boat, facing the MoO₃ powder. The system was pumped down to a pressure of 3×10^{-4} mbar and purged with 1000 sccm high purity argon for several minutes. The different thermal ramps adopted in the CVD processes are discussed in the following sections. The maximum temperature reached in the upstream furnace (tellurium region) was 800 °C and in the downstream furnace (MoO₃ region) was 850°C (see Fig.1a). The system was naturally cooled down to room temperature and 1000 sccm Ar flow was used to remove the reactants.

Sample characterization

Raman spectroscopy measurements were performed in a backscattering configuration employing a Renishaw InVia spectrometer, equipped with the 514 nm (2.41 eV) line of solid-state diode laser. The laser radiation was focused on the sample by means of a 50x Leica objective (0.75 numerical aperture), maintaining the incident laser power below 1 mW to avoid sample damage. The morphology of the sample was characterized using a Zeiss-SUPRA 40 field-emission Scanning Electron Microscope (SEM) in bright field mode. Chemical composition was probed using a XPS PHI ESCA 5600 with monochromatic Al X-rays source and hemispherical analyzer with pass energy 5.85 eV, energy step 0.025 eV and energy resolution > 0.1 eV.

Results and discussion

A thermodynamically favored condition for the emergence of a prevailing 1T' phase in MoTe₂ is known to take place when the substrate temperature is brought over 800°C as reported in case of

salt-assisted CVD.¹⁶ After setting a growth temperature of 850°C in a double furnace CVD reactor under isobaric condition (pressure of 1 atm/760 torr) and with a 10 sccm Ar/H₂ flux (H₂ 4% vol.) as a carrier gas (see **Figure 1a** for a scheme of the apparatus), we notice that an essential requirement for MoTe₂ to grow was the presence of a mechanical barrier at the downstream edge of the quartz boat hosting the substrate that serves as a physical obstacle for the vapor flux during the CVD process. This is reflected in the comparative Raman spectrum acquired after CVD growth with and without the blocking barrier in Fig. 1b. The absence of the blocking barrier gives no yield in terms of materials growth (poor Raman intensity in the spectrum), while the characteristic Raman spectrum of MoTe₂ is observed when employing the blocking barrier, which plays the role to re-direct the two main vapor fluxes (MoO₃ vapor from the boat and Ar-transported Te flux), see Fig. 1a. This scenario will be further clarified in the following while examining the effect of the Ar flux and hence, the Te transport on the MoTe₂ growth. The Raman spectrum recorded in case of a barrier-assisted CVD (see Fig. 1b, blue curve and Figure S1 in Supporting Information) exhibits well-defined peaks at 164 cm⁻¹, 107 cm⁻¹, 123 cm⁻¹ that are indicative of an interplay of domains with 1T' and 2H phases.¹⁷ The more intense peak at 164 cm⁻¹ is assigned to the B_g mode of the 1T' phase.¹⁷ Other features of the 1T' phase are the Raman peaks at 107cm⁻¹, 123cm⁻¹ and 257cm⁻¹ corresponding to the A_u, E_{1g} and A_g modes, respectively.^{18,19} The fingerprints of 2H phase of the MoTe₂ are the intense and relatively broader peaks at 230 cm⁻¹ and 180 cm⁻¹ that are assigned to the E¹_{2g}, A_g modes respectively.¹⁷ As previously proposed,¹⁸ the relative proportion of 1T' and 2H phase can be deduced by taking into account the B_g and E¹_{2g} peak intensity according to the following relations:

$$R_{1T'} = \frac{I_{B_g}}{I_{B_g} + I_{E_{2g}^1}}, \quad R_{2H} = 1 - R_{1T'}$$

Where the intensities of the Raman peaks are derived from the fit to the data as reported in Figure S1 in the Supporting Information.

The successful growth of MoTe₂ is confirmed from XPS measurements. **Figure 1 d** reports the high resolution XPS spectra from Mo(3d) and Te(4d) core levels. Considering Mo(3d) the presence of 2 Mo chemical states, each with its spin orbit splitting, is clear. We observe a Mo chemical state at binding energy 227.4 eV (5/2) and 230.6 eV (3/2) that we associate with Mo bonded with Te, to form MoTe₂.¹⁷ Further, we observe the emergence of an additional Mo chemical states at binding energies 232.5 eV (5/2) and 235.6 eV (3/2) that we attribute to oxide MoO₃. Considering Te(4d) spectral region we observe a similar situation as in Mo(3d), with the evidence of 2 Te chemical states, each with its spin orbit splitting components. In particular, we observe the presence of a Te chemical state at binding energy 39.8 eV (5/2) and 41.2 eV (3/2), that we attribute to Te bonded with Mo to form MoTe₂.¹⁷ In addition, we observe a second Te chemical states at binding energy 43.8 eV (5/2) and 45.2 eV (3/2), that we associate with the TeO₂ oxide form. In consideration of the extreme surface sensitivity of the technique, to ascertain the location of the oxidized contributions, we collected Te(3d) spectral region prior and after 1 minute Ar sputtering. As shown in **Figure S1 c** in the Supplemental Info, the peaks associated to the TeO₂ chemical state vanish after the sputtering, meaning that the oxidation is limited to the uppermost layers and the synthesized material consists of pure MoTe₂. The presence of the oxidation layer is due to the exposure to the ambient before ex-situ XPS and suggests the degree of degradation of the as-grown MoTe₂ in presence of oxygen.

The scanning electron microscopy image in Fig. 1c displays a large-area coverage of the MoTe₂ layer grown by barrier-assisted CVD that is consistent with the statistical Raman analysis vs. position. A deeper insight into the film microstructure is gained in **Figure 2 a** by high-resolution

SEM imaging of the morphological features at the microscopic level. Based on Fig. 1c and 2a, the layer is continuous on the 100 μm scale and the morphology displays a texture of crystallites with shape variability, i.e. majority rectangular domains vs minority hexagonal and triangular ones (see the insets of Fig. 2a). These characteristic geometries can be assigned to 1T' and 2H crystallites, respectively, as previously reported^{14,20} and in agreement with the concomitant presence of 1T' and 2H features in the Raman spectrum of Fig. 1b. The so-observed shape variability reflects the balance between the two MoTe₂ phases despite the growth condition is expected to be thermodynamically 1T' phase-selective. Nonetheless, in the given process scheme, we notice that the crystallite population is pretty much dominated by the rectangular crystallites, namely by a majority 1T' phase, the hexagonal shaped domain being a relatively small amount of the surface structures. The related areal distribution is then reminiscent of the nucleation mode because its statistical behavior can be rationalized by fitting functions that are influenced by different physical constraints at the early stages of the growth. This is reported as a histogram plot in Fig. 2b where the data are interpolated by means of three possible fitting functions, namely Log-normal, Γ , and Rayleigh functions. Best-fit to the data is gained with a log-normal function [$\chi^2=0.40$] with a mean value of 0.57, with slight difference from the Γ function [$\chi^2=0.75$] and a large margin with respect to the Rayleigh one [$\chi^2=8.3$], where χ^2 is the reduced chi-squared. Generally speaking, log-normal and Γ functions describe independent events (following a Poisson statistics) which are progressive, i.e. temporally separated, and simultaneous, respectively.^{21,22} As a consequence, we conclude that the experimentally derived areal distribution points out to a homogeneous nucleation where the growth of a nucleus is a random event that is independent from the others. In other words, MoTe₂ nucleation is not driven by a bias like the coalescence or preferential surface diffusion channeling nor subjected to coarsening, but it takes place at different times, with nuclei forming while other

ones are already formed. This aspect rationalizes the fact that grains with different size are observed in the grown layer.

Given the kinetic character of the nucleation and its influence on the later stages of the crystal growth, we are concerned to know how the crystallite structure can be inverted from the observed 1T' majority towards the 2H phase by changing the growth kinetics. The latter governed by CVD's dynamic parameters such as the velocity of the Te transport, which in turn can be tuned as a function of the carrier gas flux (ϕ). Indeed, ϕ is reported to play a decisive role in switching one phase from the other in the tellurization of a Mo film.¹⁰ The relevant phenomenology of vapor phase reaction as a function of ϕ , is elucidated by the Raman spectroscopic study in **Figure 3**. A positional variability of the MoTe₂ phase is observed by comparing the Raman spectra from three uniform regions in the sample (see Fig. 3a). In detail, regions 1 and 3 point out to edge zones of the samples, i.e. far from and close to the blocking barrier respectively, whereas region 2 is an intermediary zone in between the other two (see the sketch and the optical images in Fig. 3a). At low flux ($\phi = 10$ sccm) the Raman spectrum is qualified by an intense B_g peak and a minor E¹_{2g} peak therein manifesting a majority 1T' phase in the MoTe₂ structure over the whole sample (regions 1,2,3), Fig 3b. Increasing ϕ in the range 30-50 sccm leads to the emergence of a majority 2H phase (R_{1T'}=30%, R_{2H}=70%) in the proximity of the glass barrier (region 3), while a mixed phase (R_{1T'}= R_{2H}=50%) is found at region 2. Throughout region 1, a majority 1T' phase (R_{1T'}=70%) is restored, see Figure S1 b in Supporting Information. This 1T' majority condition is restored over the whole sample area increasing ϕ up to 100 sccm. The overall scenario is summarized in the histogram of Fig. 3c where R_{1T'} deduced from Eqs. 1 is plotted as a function of ϕ for region 1,2 and 3. Each point in the histogram is the average over 10 spectra taken in a mm-scaled area inside the given region where no changes appear in the optical microscope image.

The phase diagram in Fig. 3c reflects the emergence of a majority 2H phase only at $\phi=30-50$ sccm and in the proximity of the glass barrier (region 3), while the 1T' phase formation is favored ($R_{1T'}=68\%$) at flux values $\phi < 10$ sccm and $\phi > 30$ sccm in all regions detected. Basically, the observed behavior resembles a similar trend to that reported for the tellurization,¹⁰ this fact being due to the kinetic constraints for the formation of one phase when the stationary Te concentration in the reaction ambient is varied. Conversely, the positional variability can be rationalized in terms of the vapor fluid- dynamics induced by the blocking barrier with different carrier flux applied. We propose a representative picture of the barrier mechanism in Fig. 3d. In detail, in the low flux regime ($\phi = 10$ sccm), the carrier gas-assisted tellurium transport from its pristine boat to the reaction site is enough slow to give rise to a tellurium-poor environment. This Te-deficient condition induces the preferential formation of the 1T' phase throughout the whole sample area (regions 1,2, and 3, see Fig. 3d, top) consistent with the case of tellurization.¹⁰ Increasing the flux in the 30-50 sccm range results in an increased concentration of tellurium precursor in the vapor phase in the proximity of the glass barrier (region 3) thus creating the favorable condition for the 2H phase to form while farther regions (1 and 2) still suffer from a Te-deficient environment and hence, they grow with a 1T' phase, mainly (Fig. 3d, centre). The high flux regime ($\phi = 100$ sccm) reduces the residing time for the evaporating Te atoms since the Te flux is scattered back from the blocking barrier (Fig. 3d, bottom). As a consequence, no tellurium-rich atmosphere is reached in the reaction zones, thus giving rise to the 1T' phase again. The effectiveness of the convective motions is demonstrated by Te precipitation on substrate placed upstream (see Figure S2 in Supporting Information), i.e. against the carrier gas flow. As a consequence, the 2H phase occurring at low ϕ results from a Te-rich concentration and the growth dynamics is hence concentration-limited.

On the other hand, the stationary concentration of tellurium, namely the amount of Te provided during the process, is another key-parameter for the selection of a preferential phase. To get through the role of the Te concentration in the Mo-Te reaction, we vary the Te partial pressure in the flux window where the 2H phase occurs in the proximity of the glass barrier, namely at $\phi = 30$ sccm in region 3. The Te evaporation rate is controlled by means of the temperature ramp rate ΔT at the Te source while keeping the carrier gas flux at 30 sccm according to the process flow diagram in Fig. 4a. In this respect, the Te partial pressure is proportional to the evaporation rate see Fig. S3 in Supporting Information. The temperature ramp rate ΔT is varied moving on the right in the horizontal (time) scale the experimental point denoted by ‘*’ in **Figure 4a**. The Te concentration in the process is then derived as the time integral of the evaporation rate, being proportional to the triangular area A as indicated in Fig. 4a. When A is varied from 250 min*°C to 2000 min*°C (Fig.4c) a dramatical change can be observed in the characteristic features of the Raman spectrum. While at low A, the 1T'-related features definitely prevail, qualified by the emergence of dominant B_g peak in the Raman spectrum, the gradual increase of the Te concentration leads to a dominant 2H phase, Fig. 4b. As a matter of fact, qualitatively, both 1T' and 2H phases coexist throughout the whole A-range considered, with their relative abundance being adjustable by tuning the Te concentration. In order to provide a quantitative description of the phase engineering process, we report in Fig. 4c the phase proportion deduced from the Raman spectra through Eqs. (1). The fraction of the 1T' phase is calculated as the statistical mean of the $R_{1T'}$ coefficients obtained in regions 1, 2, and 3. It can be immediately noticed that the onset for a majority 2H phase formation (with $R_{2H}=80\%$) takes place at a threshold $A \geq 1500$ min*°C. For a given flux of 30 sccm, this condition stably holds on with rate amounting up to 2000 min*°C. Conversely, an almost constant $R_{1T'}=60\%$ is observed in the sub-threshold Te concentration range. Our results evidence that the

phase transitions in isothermal condition, are crucially driven by the Te concentration at the reaction point, with 2H (1T') phase resulting from a Te-rich (Te-poor) environment with the evaporating MoO₃ at the substrate, respectively. This conclusion is consistent with the concentration-limited growth condition observed in the flux dependency (see Fig. 3).

Conclusion

The chemical vapor co-deposition from MoO₃ and Te vapor effectively results in a MoTe₂ growth only when the vapor fluxes are physically blocked by a downstream positioned glass barrier. This mechanical stopper acts as a fluid-dynamics controller of the vapor reaction, thereby generating Te-poor and Te-rich conditions during the MoTe₂ nucleation. This is key-trim to dictate the phase selection in the MoTe₂ nucleation in between a semiconducting 2H phase and a topologically interesting 1T' one. In particular, the reactive co-deposition of MoTe₂ in a thermal regime where the 1T' is thermodynamically stable, discloses a kinetic scenario where the proportion of the 1T' and 2H phase is a tellurium concentration-limited mechanism. This scenario is reflected in a log-normal distribution of the crystallite grain size in the MoTe₂ film, which we rationalize as a homogeneous, random, and progressive nucleation of MoTe₂ clusters with rectangular shape (1T' phase) or hexagonal shape (2H phase). We show that these mechanisms can be readily mastered by introducing a physical barrier in the reactor thus inducing a concentration gradient of the tellurium precursor. Moreover, by tailoring the relevant process parameters, such as the temperature ramp and the carrier gas flux, the full control of the phase proportion in the grown MoTe₂ is achieved. In particular, we conclude that the environmental Te is a necessary condition to tune a Te-rich or Te-poor environment, thus leading to a dominant 2H or 1T' phase, respectively. However, not only the Te concentration matters, but also the Te transport velocity affects the Te reactivity. Overall, we succeeded in determining the kinetical conditions to have phase-selectivity

in nanoscaled MoTe₂ through a vapor phase reaction approach to the CVD toward the full phase engineering of the MoTe₂ growth down to the single layer on one hand, thus paving the way to the exploitation of phase-selected MoTe₂ for specific applications in nanoelectronics exploiting strain engineering⁵ and topological properties.^{23,24}

ASSOCIATED CONTENT

Supporting Information. The file includes additional Raman spectra of the grown material, XPS spectra after sputtering, optical picture and SEM image of the Tellurium redeposition at high carrier gas flux, the plot of tellurium vapor pressure vs time for different temperature rates in the CVD growth.

AUTHOR INFORMATION

Christian Martella, CNR-IMM, Unit of Agrate Brianza, via C. Olivetti 2, 20864 Agrate Brianza (MB) Italy <https://orcid.org/0000-0003-1811-165X>

Alessio Quadrelli, 1 CNR-IMM, Unit of Agrate Brianza, via C. Olivetti 2, 20864 Agrate Brianza (MB) Italy, 2 C.I.Ma.I.Na., Dipartimento di Fisica, Università degli Studi di Milano, Via Celoria 16, 20133 Milano, Italy.

PinakaPani Tummala, CNR-IMM, Unit of Agrate Brianza, via C. Olivetti 2, 20864 Agrate Brianza (MB) Italy

Cristina Lenardi, C.I.Ma.I.Na., Dipartimento di Fisica, Università degli Studi di Milano, Via Celoria 16, 20133 Milano, Italy.

Roberto Mantovan, CNR-IMM, Unit of Agrate Brianza, via C. Olivetti 2, 20864 Agrate Brianza (MB) Italy <https://orcid.org/0000-0002-9353-4137>

Alessio Lamperti CNR-IMM, Unit of Agrate Brianza, via C. Olivetti 2, 20864 Agrate Brianza (MB) Italy <https://orcid.org/0000-0003-2061-2963>

Alessandro Molle CNR-IMM, Unit of Agrate Brianza, via C. Olivetti 2, 20864 Agrate Brianza (MB) Italy <https://orcid.org/0000-0002-3860-4120>

Corresponding Author

Alessio Lamperti

* alessio.lamperti@mdm.imm.cnr.it

Author Contributions

All authors have given approval to the final version of the manuscript.

Funding Sources

Research partially funded with the financial support from the Horizon 2020 project SKYTOP “Skyrmion-Topological Insulator and Weyl Semimetal Technology” (FETPROACT-2018-01, n. 824123), and from Ministero dell’Istruzione, dell’Università e della Ricerca (MIUR) under the project PRIN 2017 aSTAR, grant 2017RKWTMY.

Notes

Any additional relevant notes should be placed here.

ACKNOWLEDGMENT

We acknowledge Mr. Mario Alia (CNR-IMM) for technical support. C.M. acknowledges Prof. Liu Zheng and Dr. Jiadong Zhou (Nanyang Technological University) for fruitful discussion.

REFERENCES

- (1) Zhou, L.; Zubair, A.; Wang, Z.; Zhang, X.; Ouyang, F.; Xu, K.; Fang, W.; Ueno, K.; Li, J.; Palacios, T.; Kong, J.; Dresselhaus, M. S. Synthesis of High-Quality Large-Area Homogenous 1T' MoTe₂ from Chemical Vapor Deposition. *Adv. Mater.* **2016**, *28* (43), 9526–9531. <https://doi.org/10.1002/adma.201602687>.
- (2) Zhou, J.; Liu, F.; Lin, J.; Huang, X.; Xia, J.; Zhang, B.; Zeng, Q.; Wang, H.; Zhu, C.; Niu,

- L.; Wang, X.; Fu, W.; Yu, P.; Chang, T.-R.; Hsu, C.-H.; Wu, D.; Jeng, H.-T.; Huang, Y.; Lin, H.; Shen, Z.; Yang, C.; Lu, L.; Suenaga, K.; Zhou, W.; Pantelides, S. T.; Liu, G.; Liu, Z. Large-Area and High-Quality 2D Transition Metal Telluride. *Adv. Mater.* **2017**, *29* (3), 1603471. <https://doi.org/10.1002/adma.201603471>.
- (3) Zhang, F.; Zhang, H.; Krylyuk, S.; Milligan, C. A.; Zhu, Y.; Zemlyanov, D. Y.; Bendersky, L. A.; Burton, B. P.; Davydov, A. V.; Appenzeller, J. Electric-Field Induced Structural Transition in Vertical MoTe₂- and Mo_{1-x}W_xTe₂-Based Resistive Memories. *Nat. Mater.* **2019**, *18* (1), 55–61. <https://doi.org/10.1038/s41563-018-0234-y>.
- (4) Sun, L.; Ding, M.; Li, J.; Yang, L.; Lou, X.; Xie, Z.; Zhang, W.; Chang, H. Phase-Controlled Large-Area Growth of MoTe₂ and MoTe₂-XO_x/MoTe₂ Heterostructures for Tunable Memristive Behavior. *Appl. Surf. Sci.* **2019**, *496*, 143687. <https://doi.org/10.1016/j.apsusc.2019.143687>.
- (5) Martella, C.; Mennucci, C.; Lamperti, A.; Cappelluti, E.; de Mongeot, F. B.; Molle, A. Designer Shape Anisotropy on Transition-Metal-Dichalcogenide Nanosheets. *Adv. Mater.* **2018**, *30* (9), 1705615–1705615. <https://doi.org/10.1002/adma.201705615>.
- (6) Tang, S.; Zhang, C.; Wong, D.; Pedramrazi, Z.; Tsai, H.-Z.; Jia, C.; Moritz, B.; Claassen, M.; Ryu, H.; Kahn, S.; Jiang, J.; Yan, H.; Hashimoto, M.; Lu, D.; Moore, R. G.; Hwang, C.-C.; Hwang, C.; Hussain, Z.; Chen, Y.; Ugeda, M. M.; Liu, Z.; Xie, X.; Devereaux, T. P.; Crommie, M. F.; Mo, S.-K.; Shen, Z.-X. Quantum Spin Hall State in Monolayer 1T'-WTe₂. *Nat. Phys.* **2017**, *13* (7), 683–687. <https://doi.org/10.1038/nphys4174>.
- (7) Qian, X.; Liu, J.; Fu, L.; Li, J. Quantum Spin Hall Effect in Two-Dimensional Transition Metal Dichalcogenides. *Science* (80-.). **2014**, *346* (6215), 1344–1347. <https://doi.org/10.1126/science.1256815>.

- (8) Soluyanov, A. A.; Gresch, D.; Wang, Z.; Wu, Q.; Troyer, M.; Dai, X.; Bernevig, B. A. Type-II Weyl Semimetals. *Nature* **2015**, *527* (7579), 495–498. <https://doi.org/10.1038/nature15768>.
- (9) Sun, Y.; Wu, S.-C.; Ali, M. N.; Felser, C.; Yan, B. Prediction of Weyl Semimetal in Orthorhombic MoTe₂. *Phys. Rev. B* **2015**, *92* (16), 161107. <https://doi.org/10.1103/PhysRevB.92.161107>.
- (10) Yang, L.; Zhang, W.; Li, J.; Cheng, S.; Xie, Z.; Chang, H. Tellurization Velocity-Dependent Metallic-Semiconducting-Metallic Phase Evolution in Chemical Vapor Deposition Growth of Large-Area, Few-Layer MoTe₂. *ACS Nano* **2017**, *11* (2), 1964–1972. <https://doi.org/10.1021/acsnano.6b08109>.
- (11) Vangelista, S.; Cinquanta, E.; Martella, C.; Alia, M.; Longo, M.; Lamperti, A.; Mantovan, R.; Basset, F. B.; Pezzoli, F.; Molle, A. Towards a Uniform and Large-Scale Deposition of MoS₂ Nanosheets via Sulfurization of Ultra-Thin Mo-Based Solid Films. *Nanotechnology* **2016**, *27* (17), 175703–175703. <https://doi.org/10.1088/0957-4484/27/17/175703>.
- (12) Martella, C.; Melloni, P.; Cinquanta, E.; Cianci, E.; Alia, M.; Longo, M.; Lamperti, A.; Vangelista, S.; Fanciulli, M.; Molle, A. Engineering the Growth of MoS₂ via Atomic Layer Deposition of Molybdenum Oxide Film Precursor. *Adv. Electron. Mater.* **2016**, *2* (10), 1600330–1600330. <https://doi.org/10.1002/aelm.201600330>.
- (13) Wang, X.; Gong, Y.; Shi, G.; Chow, W. L.; Keyshar, K.; Ye, G.; Vajtai, R.; Lou, J.; Liu, Z.; Ringe, E.; Tay, B. K.; Ajayan, P. M. Chemical Vapor Deposition Growth of Crystalline Monolayer MoSe₂. *ACS Nano* **2014**, *8* (5), 5125–5131. <https://doi.org/10.1021/nn501175k>.
- (14) Wang, S.; Rong, Y.; Fan, Y.; Pacios, M.; Bhaskaran, H.; He, K.; Warner, J. H. Shape Evolution of Monolayer MoS₂ Crystals Grown by Chemical Vapor Deposition. *Chem.*

- Mater.* **2014**, *26* (22), 6371–6379. <https://doi.org/10.1021/cm5025662>.
- (15) Lee, Y.-H.; Zhang, X.-Q.; Zhang, W.; Chang, M.-T.; Lin, C.-T.; Chang, K.-D.; Yu, Y.-C.; Wang, J. T.-W.; Chang, C.-S.; Li, L.-J.; Lin, T.-W. Synthesis of Large-Area MoS₂ Atomic Layers with Chemical Vapor Deposition. *Adv. Mater.* **2012**, *24* (17), 2320–2325. <https://doi.org/10.1002/adma.201104798>.
- (16) Keum, D. H.; Cho, S.; Kim, J. H.; Choe, D.-H.; Sung, H.-J.; Kan, M.; Kang, H.; Hwang, J.-Y.; Kim, S. W.; Yang, H.; Chang, K. J.; Lee, Y. H. Bandgap Opening in Few-Layered Monoclinic MoTe₂. *Nat. Phys.* **2015**, *11* (6), 482–486. <https://doi.org/10.1038/nphys3314>.
- (17) Sun, Y.; Zhuang, P.; Jiang, W.; Xu, H.; Zhang, S.; Xuan, N.; Ba, K.; Liu, H.; Wang, J.; Bao, W.; Shen, J.; Sun, Z. Phase, Conductivity, and Surface Coordination Environment in Two-Dimensional Electrochemistry. *ACS Appl. Mater. Interfaces* **2019**, *11* (28), 25108–25114. <https://doi.org/10.1021/acsami.9b03673>.
- (18) Xu, X.; Li, X.; Liu, K.; Li, J.; Feng, Q.; Zhou, L.; Cui, F.; Liang, X.; Lei, Z.; Liu, Z.; Xu, H. Thermodynamics and Kinetics Synergetic Phase-Engineering of Chemical Vapor Deposition Grown Single Crystal MoTe₂ Nanosheets. *Cryst. Growth Des.* **2018**, *18* (5), 2844–2850. <https://doi.org/10.1021/acs.cgd.7b01624>.
- (19) Empante, T. A.; Zhou, Y.; Klee, V.; Nguyen, A. E.; Lu, I.-H.; Valentin, M. D.; Naghibi Alvillar, S. A.; Preciado, E.; Berges, A. J.; Merida, C. S.; Gomez, M.; Bobek, S.; Isarraraz, M.; Reed, E. J.; Bartels, L. Chemical Vapor Deposition Growth of Few-Layer MoTe₂ in the 2H, 1T', and 1T Phases: Tunable Properties of MoTe₂ Films. *ACS Nano* **2017**, *11* (1), 900–905. <https://doi.org/10.1021/acsnano.6b07499>.
- (20) Sung, J. H.; Heo, H.; Si, S.; Kim, Y. H.; Noh, H. R.; Song, K.; Kim, J.; Lee, C.-S.; Seo, S.-Y.; Kim, D.-H.; Kim, H. K.; Yeom, H. W.; Kim, T.-H.; Choi, S.-Y.; Kim, J. S.; Jo, M.-H.

- Coplanar Semiconductor–Metal Circuitry Defined on Few-Layer MoTe₂ via Polymorphic Heteroepitaxy. *Nat. Nanotechnol.* **2017**, *12* (11), 1064–1070. <https://doi.org/10.1038/nnano.2017.161>.
- (21) Bergmann, R. B.; Bill, A. On the Origin of Logarithmic-Normal Distributions: An Analytical Derivation, and Its Application to Nucleation and Growth Processes. *J. Cryst. Growth* **2008**, *310* (13), 3135–3138. <https://doi.org/10.1016/j.jcrysgro.2008.03.034>.
- (22) Fátima Vaz, M.; Fortes, M. A. Grain Size Distribution: The Lognormal and the Gamma Distribution Functions. *Scr. Metall.* **1988**, *22* (1), 35–40. [https://doi.org/10.1016/S0036-9748\(88\)80302-8](https://doi.org/10.1016/S0036-9748(88)80302-8).
- (23) Safeer, C. K.; Ontoso, N.; Ingla-Aynés, J.; Herling, F.; Pham, V. T.; Kurzmann, A.; Ensslin, K.; Chuvilin, A.; Robredo, I.; Vergniory, M. G.; de Juan, F.; Hueso, L. E.; Calvo, M. R.; Casanova, F. Large Multidirectional Spin-to-Charge Conversion in Low-Symmetry Semimetal MoTe₂ at Room Temperature. *Nano Lett.* **2019**, *19* (12), 8758–8766. <https://doi.org/10.1021/acs.nanolett.9b03485>.
- (24) Liang, S.; Shi, S.; Hsu, C.; Cai, K.; Wang, Y.; He, P.; Wu, Y.; Pereira, V. M.; Yang, H. Spin-Orbit Torque Magnetization Switching in MoTe₂/Permalloy Heterostructures. *Adv. Mater.* **2020**, *32* (37), 2002799. <https://doi.org/10.1002/adma.202002799>.

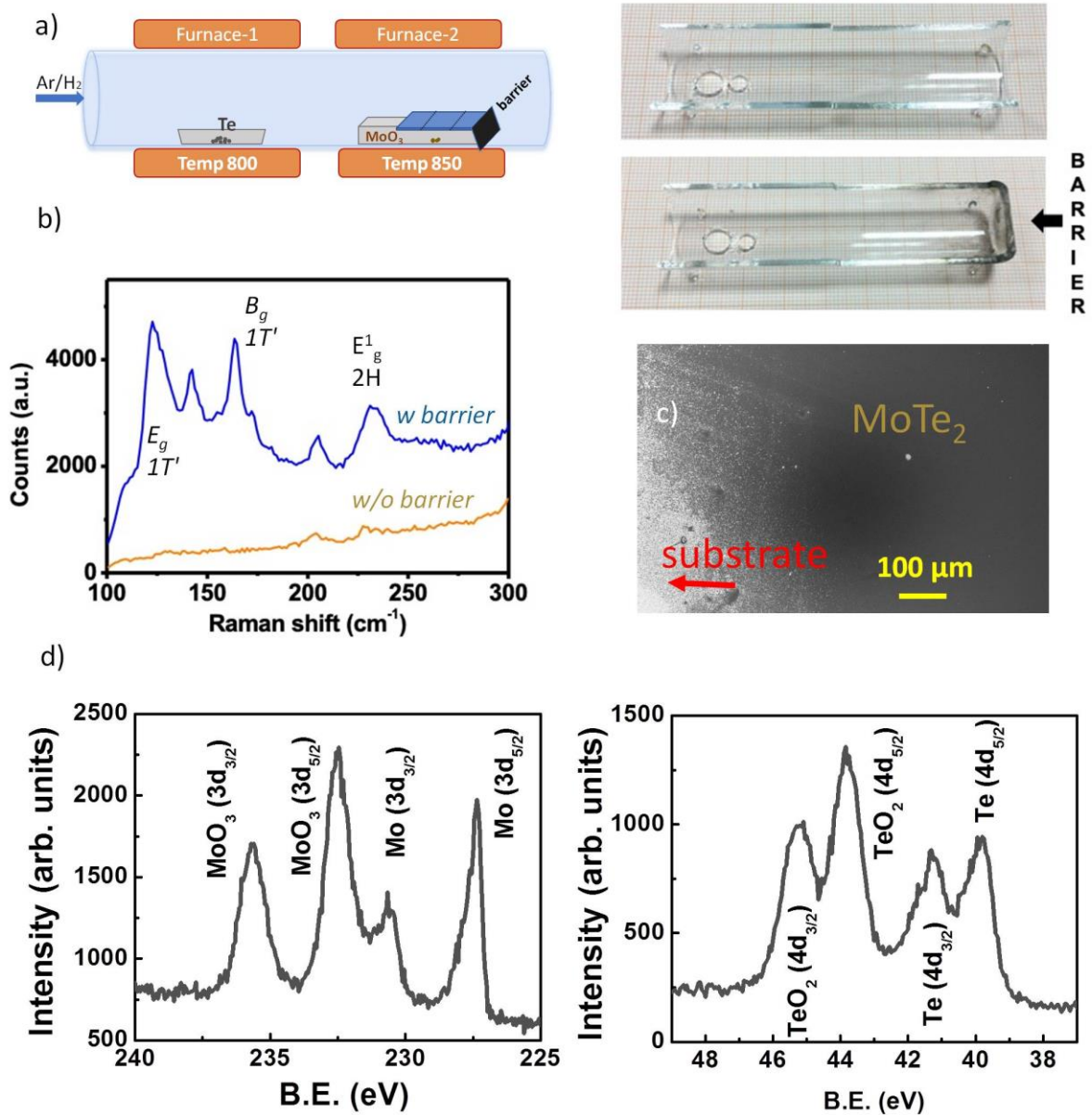


Figure 1 a) Schematic view of the experimental setup for the barrier-assisted CVD growth of MoTe₂ films. On the right, glass boat containing the MoO₃ powder and the substrate without the glass barrier (top) and with the barrier (bottom). b) Raman spectra of the MoTe₂ film obtained with (blue trace) and without (orange trace) barrier. c) Large area SEM image of the MoTe₂ film obtained by the barrier-assisted CVD approach. d) Mo (3d) and Te (4d) spectral regions from

XPS; the oxide component is coming from thin layer at the surface due to atmosphere exposure
(see Supplemental Info).

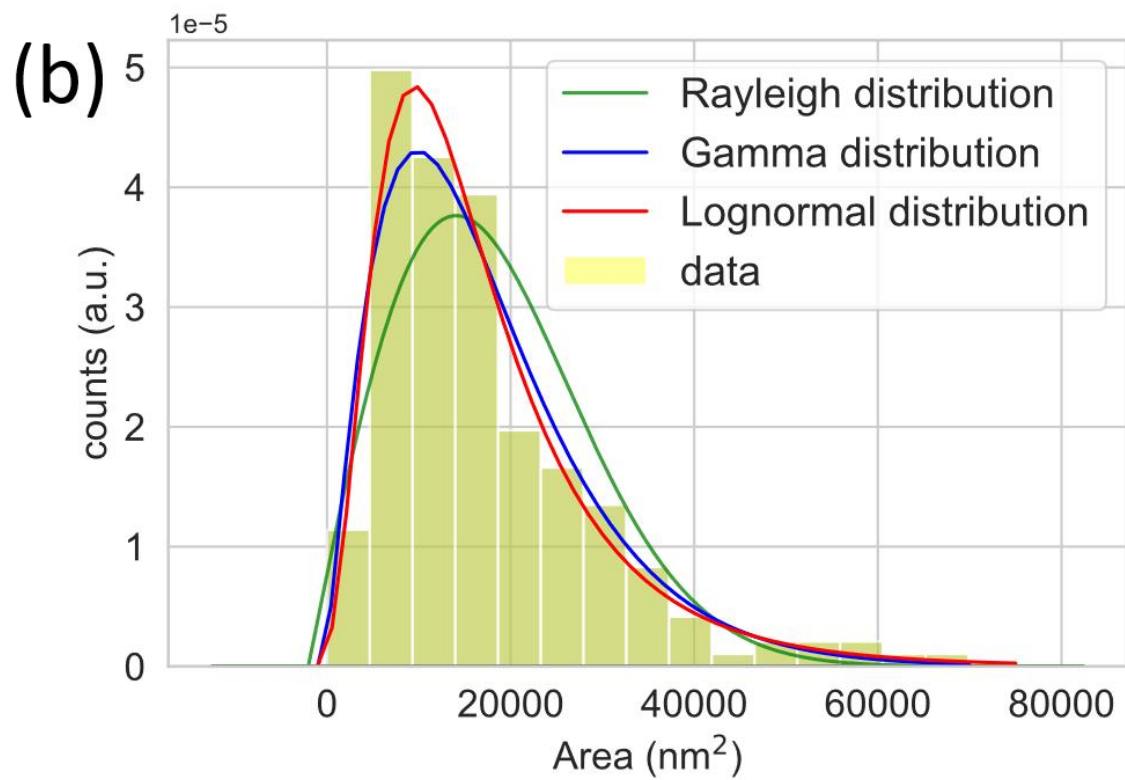
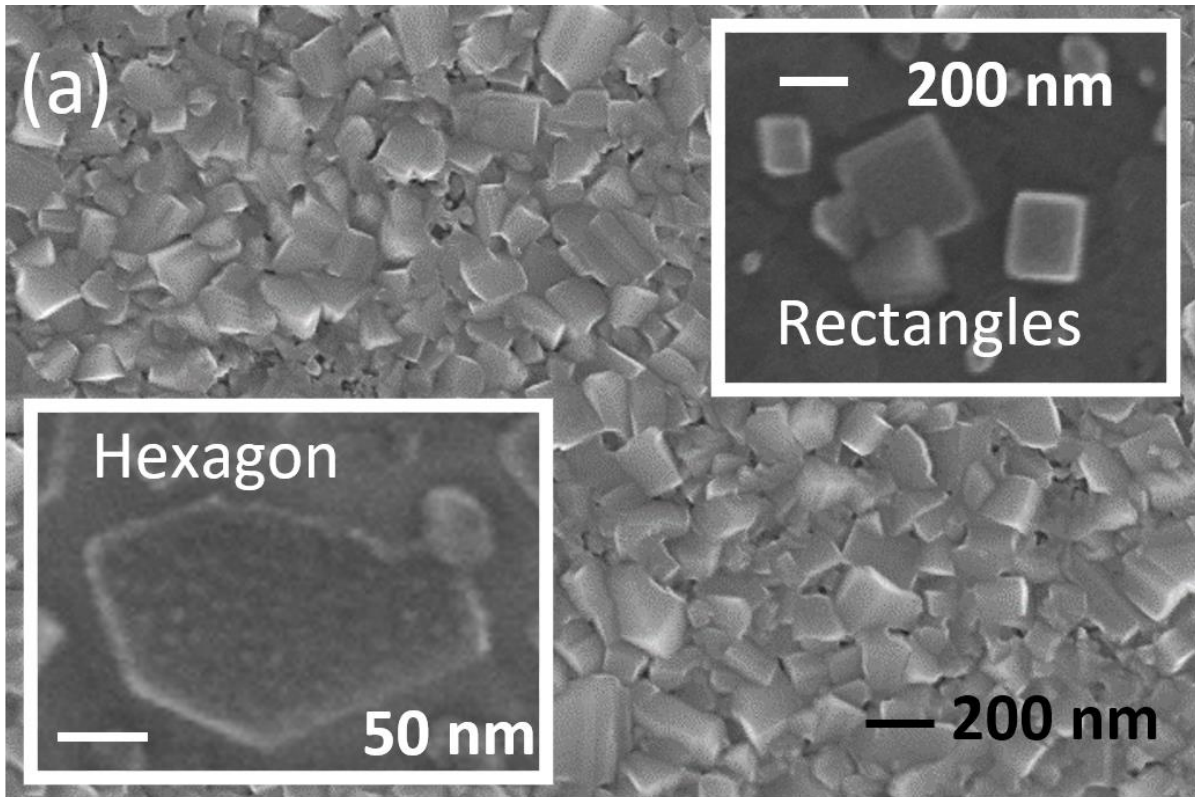


Figure 2 a) Large area and high resolution (insets) SEM images showing the MoTe₂ crystallites with the characteristic rectangular and hexagonal shapes. b) Histogram of the crystallite area distribution fitted to Rayleigh, Gamma and Lognormal distributions.

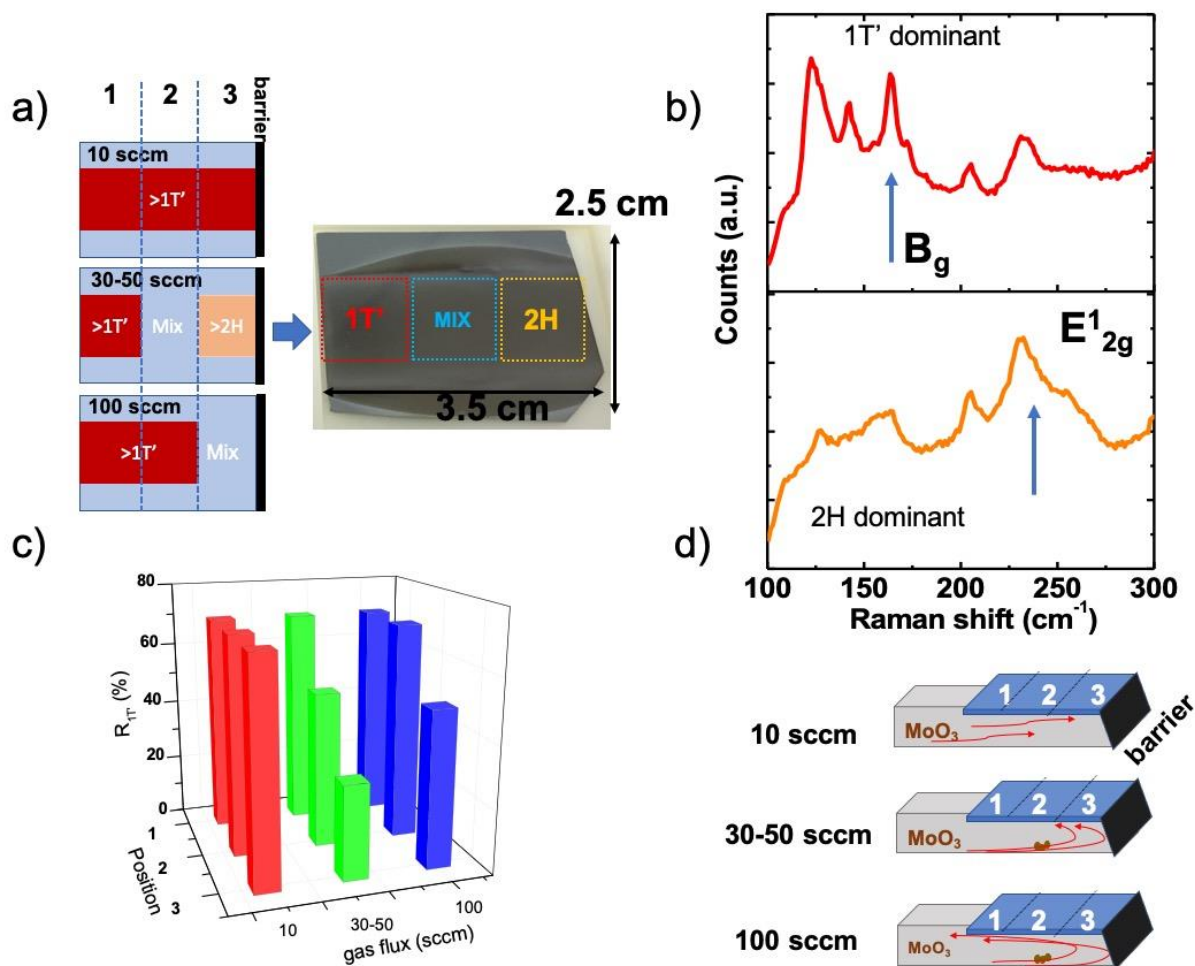


Figure 3 a) Schematic and optical view of the samples b) Raman spectra showing respectively the dominant 1T' (red) or 2H (orange). c) Histograms of the relative 1T' proportion in the samples as a function of the carrier gas flux and position 1,2,3 on the sample surface as shown in

panel a). d) Sketches of the barrier induced Te concentration mechanism as a function of the gas flux.

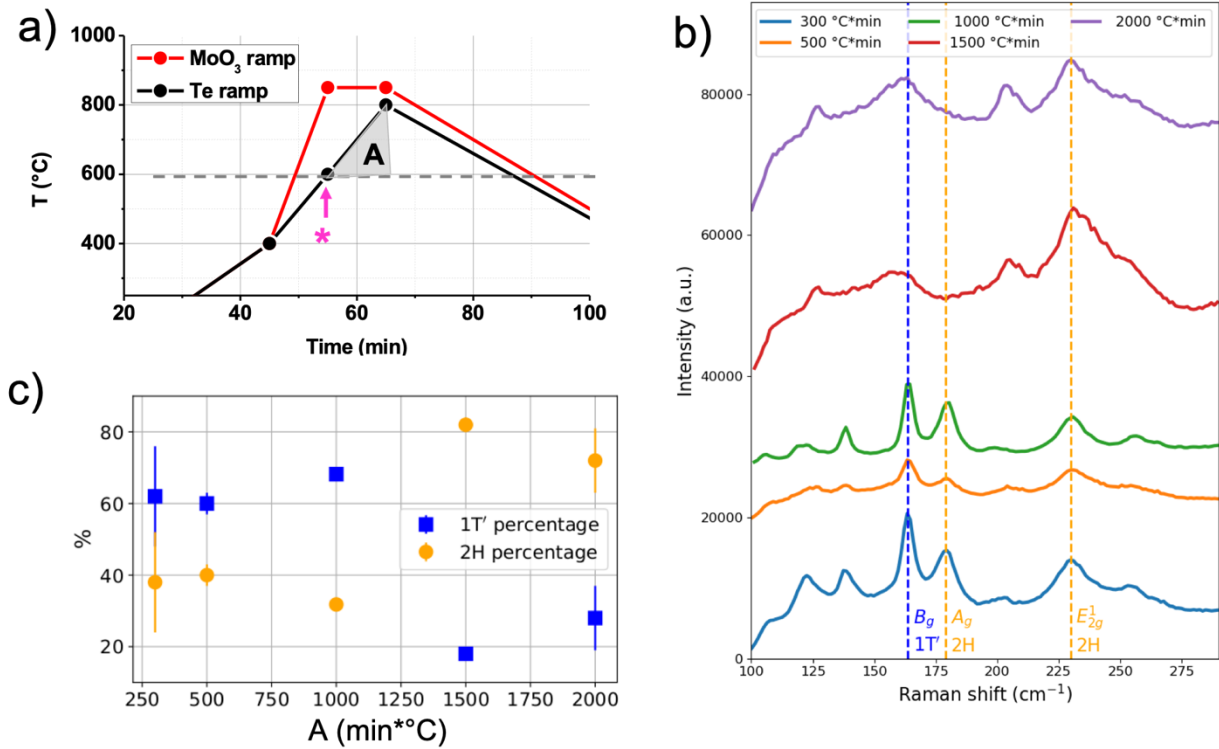


Figure 4 a) Thermal ramps of the MoTe₂ growth. The integral tellurium concentration provided throughout the growth is proportional to the area of the triangle denoted by A. Moving the experimental point “*” on the right in the time scale, the area of the triangle is varied. b) Raman spectra at different integral Te concentration c) Relative proportion of 1T' and 2H phase as a function of the integral tellurium concentration provided throughout the growth.